Multiscale aeroelastic simulations of large wind farms in the atmospheric boundary layer

Athanasios Vitsas, Johan Meyers

Department of Mechanical Engineering, KU Leuven, B-3001 Leuven, Belgium

E-mail: athanasios.vitsas@kuleuven.be, johan.meyers@kuleuven.be

Abstract. In large wind farms, the turbulence induced by each turbine results in high overall turbulence levels that can be detrimental for downstream wind turbine components. In the current study, we scrutinize structural loads and dynamics, and their correlation to turbulent flow structures by conducting aeroelastic simulations in wind farms. To this end, a pseudospectral large-eddy simulation solver is coupled with a multibody dynamics module in a multiscale framework. The multirate approach leads us naturally to the development of an aeroelastic actuator sector model that represents the wind turbine forces on the flow. This makes it computationally feasible to simulate long time horizons of the two-way coupled aeroelastic system. Hence, it allows us to look at the interaction of the turbine structure with the turbulent boundary layer and the wakes of multiple turbine arrays, and to get estimates of damage equivalent loads and structural loading statistics, as longer time series are available. Results are shown for two typical wind farm layouts, i.e. aligned and staggered, for above-rated flow regimes.

1. Introduction

Optimal layout and/or coordinated control of power maximization and loads alleviation of large wind farms can significantly cut down the overall cost of wind energy [1–4]. The design and control engineers could be facilitated by gaining adequate insight into the complex dynamic interactions that take place among the clustered turbines. This necessitates the use of high-fidelity multiphysics tools that can represent authentic flow patterns and accurate structural response. To this end, we rely on large-eddy simulations (LES) coupled with flexible multibody simulations (MBS), offering us a well-balanced trade-off between computational time and fine-scale resolution.

Substantial research has focused on the parametrization of the wind turbines in LES, namely the most widespread approaches are the actuator disk (ADM) [5–9] and line method (ALM) [10–14]. Those wind turbine models are preferred since it is still computationally prohibitive to conduct large-eddy simulations of extensive wind farms with fully-resolved turbine geometry. Lately other variants have been introduced such as the actuator surface [15] and sector model [16] attaining improved accuracy or lower computational cost.

Limited studies exist that deal with the fluid-structure interaction (FSI) of wind turbine arrays in an LES framework, even though the loads and the performance may vary significantly due to the flexibility of the modern wind turbines [17]. In Ref. [18] one array of 16 turbines is simulated using four different models including one aeroelastic ALM, where the EllipSys3D flow solver is loosely coupled with the aeroelastic code Flex5 [19]. In Ref. [20] a conventional staggered

coupling approach is applied between the research LES code SnS and the aero-elastic software FAST (Fatigue, Aerodynamics, Structures and Turbulence) [21] in a two-turbine setup. The LES time step varies between 0.06 and $0.2s$ while the time step of FAST is fixed to $0.01s$, hence a sub-cycling procedure takes place for the structural dynamics. At the end of those cycles the blade loads are averaged over annular rings and then added to the flow in a generalized actuator disk manner. The same authors developed an actuator sector approach for rigid blades to relax the time step constraints associated with the actuator line model [16], and later they applied it to flexible turbines [22]. In other work, FAST is coupled with the open-source CFD software OpenFOAM [23] to form the SOWFA tool (Simulator fOr Wind Farm Applications) [24]. In Ref. [24], the impact of neutral and unsteady atmospheric stability on the structural loads of a two-turbine array is evaluated. In the same study, the time step is restricted to $0.02s$ such that the blade motion is captured and the tip of the actuator lines does not exceed more that one grid cell per time step. Recently, a sweeped actuator line model similar to the actuator sector model [16] was included in SOWFA to deal with the ALM temporal constraints [25].

In the current work we implement a two-way partitioned FSI coupling where the turbine forces are represented by the sector area that is swept by elastic blades during one LES time step. Our approach is conceptually similar to that of Refs. [16, 25] but with certain distinctive details. In Ref. [25] the velocity is sampled at the last blade position and then this field is used for the evaluation of the loads at the intermediate positions of the sector, while in Ref. [16] the velocity is sampled at the average azimuth position. In the current work, the velocity is sampled in every sub-step based on the actual blade position. In the implementation of Ref. [16] the distribution of the forces in the sector is convolved with a box kernel with a filter width related to the sector angle. In our work, we use a first-order low-pass temporal filter instead that results in a force distribution resembling the blade motion through the sector.

More details on the coupling scheme are given in Section 2.3, after introducing the turbulent flow and multibody dynamics solvers in Sections 2.1 and 2.2 respectively. In Section 3 we present aeroelastic simulations of an aligned and a staggered wind farm layout where we look into the interactions that take place in the different rows of the farm. We also discuss the effect of the layout on the performance, the damage equivalent loads and the structural response.

2. Methodology

2.1. Fluid problem

Large-eddy simulations are conducted using our in-house code SPWind [7] that combines a Fourier pseudospectral method in streamwise and spanwise direction with a fourth-order finite difference scheme in the vertical direction. The time is advanced using the fourth-order classical variant of the Runge-Kutta method, and the time step satisfies a Courant-Friedrichs-Lewy number equal to 0.4. Precursor simulations of a thermally neutral pressure-driven boundary layer with shifted periodic boundary conditions serve as an inflow for the main wind farm domain [26]. The flow problem is governed by the LES-filtered incompressible continuity and Navier-Stokes equations, i.e.

$$\boldsymbol{\nabla} \cdot \widetilde{\mathbf{u}} = 0, \tag{1}$$

$$\frac{\partial \widetilde{\mathbf{u}}}{\partial t} + \widetilde{\mathbf{u}} \cdot \nabla \widetilde{\mathbf{u}} = -\frac{1}{\rho} \nabla \bar{p} + \boldsymbol{\nabla} \cdot \tau_{\mathbf{M}} + \bar{F} \tag{2}$$

where, $\widetilde{\mathbf{u}}$ is the resolved velocity field, $\bar{p}$ is the pressure field, and ρ is the air density. Furthermore, $\tau_{\mathbf{M}}$ are the subgrid-scale stresses that are modelled using the standard Smagorinsky model with a constant coefficient of $C_s = 0.14$ in combination with the Mason and Thomson's damping function close to the wall [27]. Finally, $\bar{F}$ represents the influence of the turbine forces on the flow (see Subsection 2.3).

2.2. Structural problem

The finite-element floating frame of reference (FFR) formulation [28] is employed for the deformation analysis of the flexible bodies of tower and blades. In the FFR approach, each body is described by the reference coordinates that specify its position and orientation, and the elastic coordinates that define its deformation with respect to the body coordinate system. The advantage of this formulation is that in the body reference frame a linear problem can be solved, thus modal reduction techniques can be applied. However, the coupling between the reference motion and the elastic deformation leads to a highly non-linear inertia matrix [29]. In this work, the orientation of the rotor's body reference frame is described by using the Bryant angles, but only the rotation around the low-speed shaft is assumed to contribute to the dynamic behaviour. Therefore, tilting and yawing are taken into account quasi-statically. The governing equations of motion for the multibody system can be written as [28]

$$\mathbf{M}(\boldsymbol{q})\ddot{\boldsymbol{q}} + \mathbf{C}\dot{\boldsymbol{q}} + \mathbf{K}(\boldsymbol{q})\boldsymbol{q} + \boldsymbol{\Phi}_{\mathbf{q}}^{\top}\boldsymbol{\lambda} = \boldsymbol{Q}_{\boldsymbol{a}} + \boldsymbol{Q}_{\boldsymbol{g}} + \boldsymbol{Q}_{\boldsymbol{v}} \tag{3}$$

$$\boldsymbol{\Phi}(\boldsymbol{q}) = \mathbf{0} \tag{4}$$

where, $\mathbf{M}$, $\mathbf{C}$, $\mathbf{K}$, are the mass, damping and stiffness matrices respectively for which the required structural properties are given in the specification file of the NREL 5-MW wind turbine [30]. The stiffness matrix $\mathbf{K}$ is composed of a constant three-dimensional Euler-Bernoulli beam stiffness matrix [31] and a nonlinear geometric stiffness matrix that couples the axial and transverse displacements [32]. The vectors $\boldsymbol{q}$, $\dot{\boldsymbol{q}}$, $\ddot{\boldsymbol{q}}$ are the generalized coordinates and their first and second time derivative, $\boldsymbol{\Phi}_{\mathbf{q}}$ is the constraint Jacobian matrix, and $\boldsymbol{\lambda}$ are the Lagrange multipliers. Constraint equations are applied between the different body coordinate systems and are expressed by the algebraic relations of Eq. (4). Furthermore, $\boldsymbol{Q}_{\boldsymbol{a}}$ and $\boldsymbol{Q}_{\boldsymbol{g}}$ represent the aerodynamic and gravitational loads respectively, while the Coriolis and gyroscopic loads are included in the non-linear quadratic velocity vector $\boldsymbol{Q}_{\boldsymbol{v}}$ [28]. For the controlled degree of freedom (DOF) of the rotor's revolution, the speed is regulated to a desired nominal value by adjusting the generator torque demand, while in region III of the turbine's operation a standard PI controller regulates the pitch angle [33].

An eigenvalue problem is solved first in the absence of damping and external loading so as to extract the mode shapes and natural frequencies of the turbine structure. Then, a common modal transformation technique is applied to the elastic coordinates to reduce the order of the model. We use two side-to-side and two fore-aft modes for the tower, while for the blades we select two flapwise, two edgewise, one torsional and one axial mode. The resulting mode shapes, natural frequencies and steady-state response are in very good agreement with the documented values of the turbine's manual [30].

The reduced system of the DAEs is integrated into time employing the generalized-α method [34]. The time step is fixed to $0.01s$ and the spectral radius parameter of this temporal discretization scheme is set to 0.9 which amounts to low numerical damping [34].

2.3. Aeroelastic actuator sector model

The complex shape of the wind turbine components require an enormous amount of grid points to fully resolve detailed phenomena such as flow separation occurring on its geometry. This translates to a high computational cost especially if one uses a relatively expensive turbulence model such as LES and simulates multiple turbines in a large domain. This leaves us with no option but to use one of the actuator methods that have already been mentioned in the introduction. Specifically the ALM seems the most straightforward option out of them to couple the fluid-structure interaction problem. However, an accurate representation of the rotor loads and wake is achieved under the condition that the blade tip motion does not exceed more than one mesh cell per time step. Additionally, the computation of the structural oscillations requires

a fine time scale, much finer than the one required for the flow equations that need simply to satisfy the CFL condition. Since the CFD computation is far more compute intensive than integrating the structural equations of motion, a sub-cycling process is being employed [35].

The procedure of the aeroelastic coupling is illustrated in Figure 1. The relative velocity V_{rel} is evaluated based on the interpolated induced velocity field $\hat{u}$ at the airfoil's deflected position, and on the blade's out-of-plane $\dot{q}_{OoP}$ and in-plane $\dot{q}_{iP}$ motion. The flow angle ϕ between V_{rel} and the plane of rotation can be determined from trigonometry of the involved velocity triangle (see Figure 1a), and it can then be decomposed to the pitch angle β (the initial twist of the blade is also included here), to the torsional deflection τ and to the angle of attack α.

The lift L and drag D forces, and the pitching moment M can then be determined from tabulated 2D airfoil data, and therefore the projected normal F_N and tangential forces F_T are computed for every sub-cycle m (Figure 1b). Note that the airfoil data have been corrected to include three-dimensional effects according to Ref. [30], yet in this work we don't include any dynamic stall characteristics. The number of sub-cycles N_s is defined by the LES time step Δt, the Runge-Kutta stage i, and the fixed stepsize of the structural equations δt. At sub-iteration m the forces F_N^m and F_T^m are calculated based on the velocity field u^m that is interpolated between the Runge-Kutta stages depending on the blade's position in the sector and the deflection q^m (see Figure 1c). The loads serve as an input to the equations of motion (see Eq. 3) that are solved in every sub-step updating the turbine's motion. The drag forces acting on the nacelle and the tower are computed only in one sub-iteration, and subsequently added to the flow equations using a Gaussian filter.

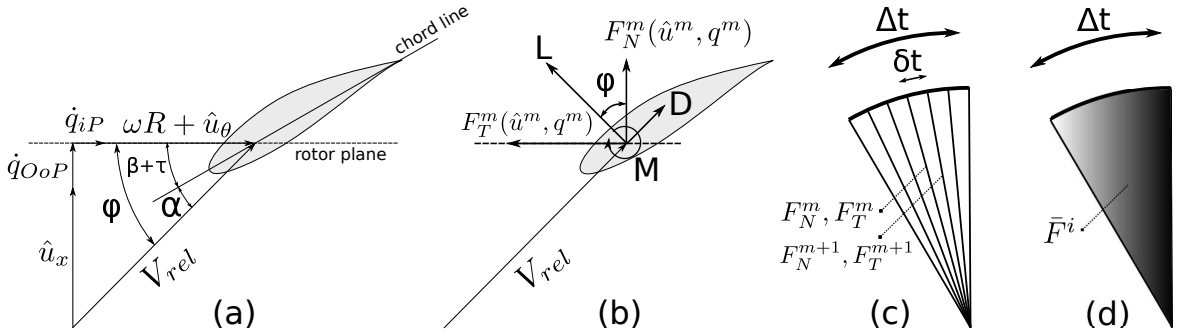

Figure 1. The aeroelastic actuator sector model comprises of the steps: (a) evaluation of the angle of attack from the airfoil's cross-section velocity triangle and blade's motion, (b) the local cross-section forces are computed from 2D airfoil data, (c) the blades sweep a sector area using a sub-cycling scheme, and (d) the sector area forces are time-filtered (spatial filtering that precedes is not depicted). The color grading in (d) denotes that more weight is given to the forces in the end position rather than in the first sub-cycle.

During each LES time step, the blades sweep a sector area evaluating the loads and its dynamic response. The sector forces need to be added to the flow, so that the solution takes into account the presence of the blades within this trajectory. The body forces are added to the flow equations after being time and spatially filtered. First, the unsteady forces $F(\hat{u}, q)$ are smeared out in the surrounding LES mesh nodes by taking their convolution with a Gaussian kernel G_n, resulting in the spatially filtered forces $\hat{F}(x)$:

$$\hat{F}(\mathbf{x}) = \sum_{n=1}^{N_t} \sum_{j=1}^{N_b=3} \int_0^R F(\hat{u}, q, r) G_n(\|\mathbf{x} - r\mathbf{e_j}\|) dr \tag{5}$$

where, N_t is the number of turbines, N_b the number of blades, and $\|\mathbf{x} - r\mathbf{e_j}\|$ is the Euclidean distance between the LES grid point and the deflected actuator line point, completing this way the two-way FSI coupling.

The body forces $\bar{F}$ of the Navier-Stokes equations (see Eq. 2) are then calculated by time-filtering the Gaussian-filtered forces $\hat{F}$. Therefore, we adopt a first-order low-pass filter which gives more weight to the last sub-iterations (see Figure 1d). The time-filter is then given as follows:

$$\frac{d\bar{F}^i}{dt} = \frac{1}{\tau_f}\left[\hat{F} - \bar{F}^i\right] \tag{6}$$

where, $\bar{F}^i$ is the time-filtered force at Runge-Kutta stage i, $\hat{F}$ are the spatially filtered forces through the sub-cycles, and τ_f is the time filter constant. The filter constant τ_f defines the effective sector angle, and here we choose it to be equal to the LES time step. Equation 6 is integrated during sub-iterations using an implicit Euler scheme as follows

$$\bar{F}^{i,m} = (1-\gamma)\bar{F}^{i,m-1} + \gamma\hat{F}^m, \qquad m = 1, \ldots, N_s \tag{7}$$

where, the filter parameter γ is given by $\gamma = \delta t/(\tau_f + \delta t)$. Subsequently, $\bar{F}^i$ is marched into the LES time scale following the Runge-Kutta scheme. The algorithmic process that was discussed in this subsection is given in Algorithm 1. Note that the number of sub-iterations is different for each Runge-Kutta stage, and that for the multibody dynamics we keep the solution of the last stage where the full sector is swept. Alternatively, an extra computation of the structural equations could be carried out after the final update of the velocity by interpolating the fields between $u^{(n)}$ and $u^{(n+1)}$.

for *Runge-Kutta stage i=1,4* **do**
  for *sub-iteration m=1,N_s* **do**
    foreach *blade element* **do**
      Interpolate velocity $\hat{u}^m = linearInterp(u^{(i)}, u^{(n)}, q^{i,m})$;
      Compute forces $F^m(\hat{u}, q^{i,m}, r) = (F_N^m, F_T^m)$;
    end
    MBS solver (Eq. 3 & 4): $\rightarrow q^{i,m+1}, \dot{q}^{i,m+1}, \ddot{q}^{i,m+1}$;
    Gaussian-filter (Eq. 5) $\rightarrow \hat{F}^m$;
    Time-filter (Eq. 7) $\rightarrow \bar{F}^{i,m}$;
  end
  Update Navier-Stokes body-force term (Eq. 2): $\bar{F}^i \leftarrow \bar{F}^{i,N_s}$;
  Compute RHS of the time-filter equation: $R^i = \frac{1}{\tau_f}(\hat{F}^{N_s} - \bar{F}^{(n)})$;
end
$\bar{F}^{(n+1)} = \bar{F}^{(n)} + \Delta t \cdot \sum_{i=1}^{4} \beta_i R^i$;
$q^{(n+1)} = q^{(i=4)}, \dot{q}^{(n+1)} = \dot{q}^{(i=4)}$;

Algorithm 1: The pseudocode of the aeroelastic actuator sector procedure.

2.4. Computational set-up

A main computational domain of size $4\pi \times \pi \times 1\,km$ is discretized by $512 \times 192 \times 125$ grid points. The wind farm consists of 32 NREL 5-MW horizontal-axis wind turbines (HAWT) of rotor diameter equal to $D = 126\,m$ and hub-height of $z_h = 90\,m$ [30]. Four turbines are placed in each row, with a spacing between the rows and columns of turbines equal to $7 \times 6.2\,D$ respectively.

Two typical wind farm layouts are examined, i.e. aligned and staggered. An above-rated flow regime of a hub-height velocity equal to $U_{hub} = 16.6\,m/s$ is simulated for 90 minutes of turbine operation. The LES time step is approximately $0.4\,s$ which corresponds to a sector angle of 29° that is swept in about 40 sub-iterations.

The precursor simulation is of equal size and spacing. The atmospheric boundary layer (ABL) is solved in the precursor simulation using a surface roughness length $z_0 = 0.1\,m$ that is a typical value for onshore conditions. The initial logarithmic profile was let to reach a statistical equilibrium for 22 hours which is comparable to 105 flow-through times. This spin-up field was used afterwards as the starting point for both the windfarm and ABL simulation of the two computational domains. The simulations are performed using 400 cores of Ivy Bridge architecture, and the wall clock time of the calculation is 140 hours.

3. Results and discussion

3.1. Flow field and turbine performance

Contour plots of the normalized time-averaged velocity field on an horizontal plane at the hub level of the two wind farm layouts are illustrated in Figure 2. The magnitude of the velocity is normalized with the horizontally-averaged hub-height velocity which is approximately $U_{hub} = 16.6\,m/s$. Streaks of high wind speed cross the aligned wind farm without being obstructed by any wind turbine, while in the staggered case less high-speed streaks are observed between the turbine columns.

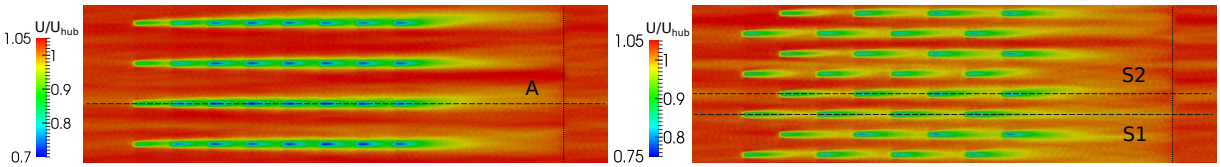

Figure 2. Normalized time-averaged velocity field at hub-height for the aligned (left) and the staggered (right) wind farm layout. The dotted lines represent the outset of the fringe region, while the dashed lines denote the aligned (A) and the two possible staggered (S1, S2) columns.

The hub-height velocity is plotted in Figure 3 with respect to the streamwise coordinate. The hub-height velocity is averaged among the columns A, S1, S2 that are defined in Figure 2. The velocity deficit created downstream of the turbines is higher in the aligned case than in the staggered cases, except for the first row. In the first row, the staggered columns of the odd rows (S1) of the wind farm experience almost the same velocity decrease with the aligned ones. The effective distance between two rows is double in the staggered wind farm and the wake is almost depleted when it reaches the next row, thus higher velocities exist in this configuration.

The hub-height velocity is above the rated wind speed ($U_{rated} = 11.4\,m/s$ [30]) for all the turbines, therefore all of them are operating in region III and produce the nominal power. As was mentioned in Section 2.2 a typical PI controller is employed to regulate the rotor's speed to the rated value by pitching the blades in region III. In Figure 4 the mean and the standard deviation of the pitch angle per row is shown. The mean pitch value reveals that more pitching is required in the staggered configuration due to the higher wind speeds. Furthermore, less pitch activity is present since the staggered turbines are not affected as much by the fluctuating velocity components of the upstream turbulent wakes as the aligned ones.

3.2. Structural loads and response

We use the damage equivalent loads (DELs) to compare the relative difference between various load histories in different turbine rows and layouts. They are derived using the Palmgren-

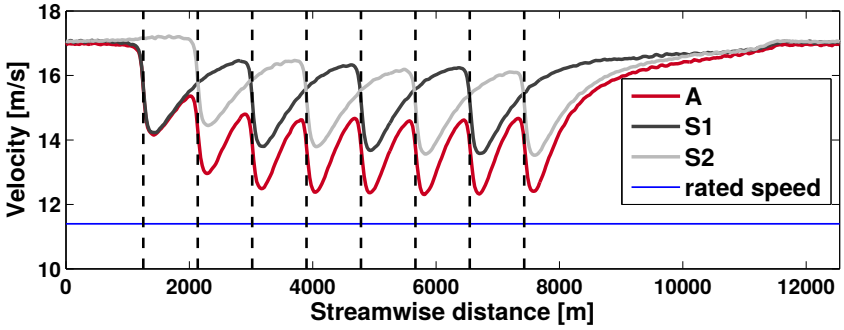

Figure 3. Velocity magnitude at hub-height as a function of the streamwise distance. The velocity is averaged over the aligned columns (A), the staggered columns of the odd rows (S1) and the staggered columns of the even rows (S2). The vertical dotted lines correspond to the eight rows of turbines.

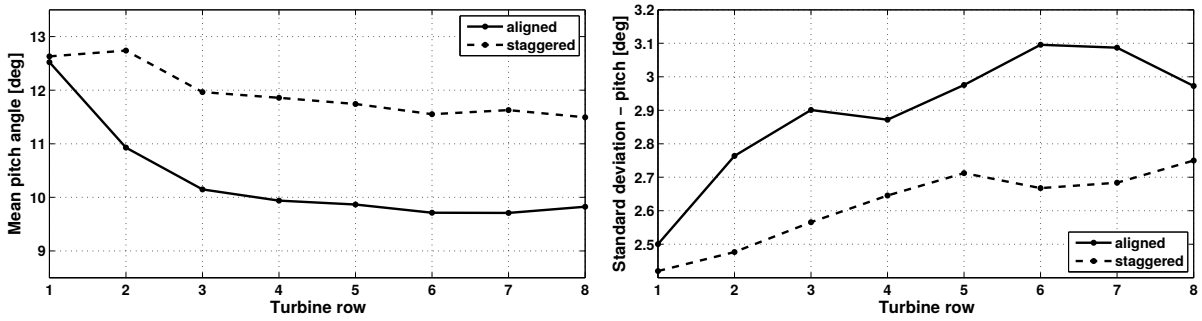

Figure 4. Mean value (left) and standard deviation (right) of the blades pitch angles averaged per row for the two wind farm configurations.

Miner rule that accounts for the accumulating fatigue damage caused to the wind turbine components by the alternating variable-amplitude structural loads, further also using the Wöhler equation [36]. The loads time series are counted and binned into individual cycles using the rainflow-counting algorithm [37], and the components follow the Wöhler's curve with a slope coefficient equal to 10 (fiberglass composite blades) [38].

The damage equivalent loads (DELs) of the out-of-plane blade root bending moment M_{OoP} are averaged per row and are compared in Figure 5 for the two wind farms. In both cases the downstream turbines have higher DELs than the first row due to the induced turbulence that causes the loads to fluctuate around higher mean values and with larger amplitudes. This is confirmed by the matrix of the rainflow counted cycles (see Figure 6) where one first row turbine is compared with a last row turbine in each layout. The aligned turbines experience higher fatigue loading than the staggered due to the fact that their velocity is closer to the rated speed where the thrust force is maximum. The staggered turbines, as shown above, have larger pitch angles. Hence the projected normal forces and the DELs of the blade root bending moment are lower.

The power spectral density of the blade root bending moment is plotted in Figure 7 for a first and a last-row turbine of the aligned case. The typical peaks in the once-per-revolution frequency and its multiples related to effects such as wind shear and tower shadow are occurring here as well. Interestingly, in the low-frequency spectrum of the last-row turbine several peaks can be associated with the total time spent for the flow to be convected from another upstream

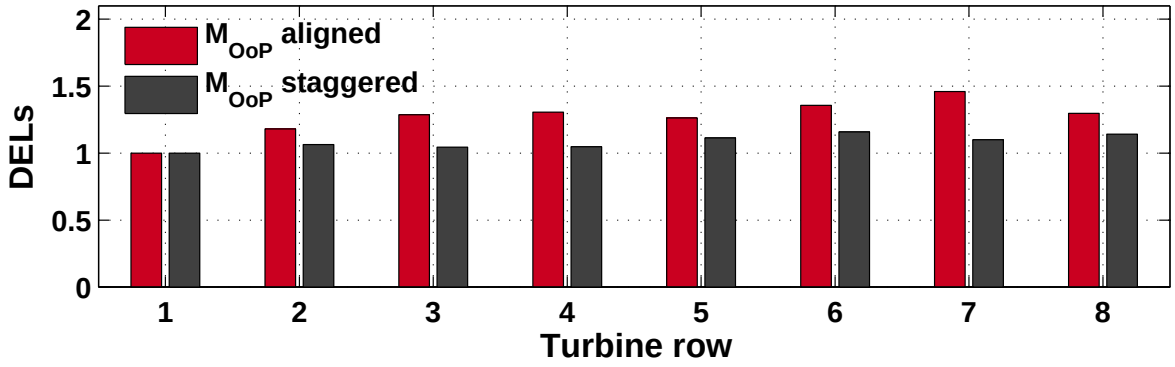

Figure 5. Comparison of the normalized DELs (left) of the out-of-plane (M_{OoP}) blade root bending moments between the aligned and the staggered wind farm configuration.

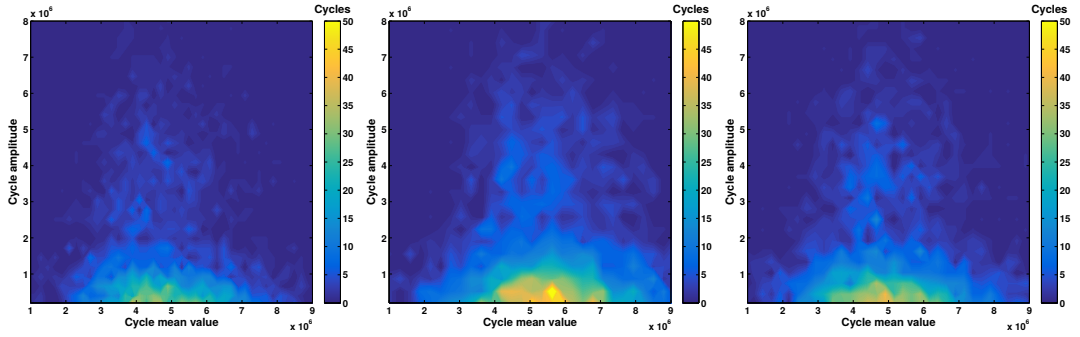

Figure 6. Rainflow-counting matrix of the out-of-plane blade root bending moments of a first-row turbine (left), a last-row turbine of the aligned wind farm (center) and a last-row turbine of the staggered layout (right). The colorbar indicates the number of cycles of a certain load amplitude bin.

row to the last one, implying strong correlations between the different turbines rows [39].

Regarding the structural response of the turbine, the mean value and the standard deviation of the blades tip deflection is shown in Figure 8 for the two wind farm configurations. As can be expected, the deflection follows the trend of the bending moments, where also larger values are discerned for the aligned turbines.

4. Conclusion

An aeroelastic actuator sector model was proposed in this study that enabled us to efficiently include FSI effects in large wind farm studies. The impact of the turbulent structures and wakes on the structural response of flexible wind turbines was assessed using two wind farm configurations. The damage equivalent loads were increasing downstream of the first row for both wind farms by virtue of increasing turbulence levels. The staggered wind farm was subjected to less fatigue loads due to the longer effective distance between turbine rows allowing the wake to almost recover before reaching the next turbine row. This means that higher hub-height velocity was seen by the staggered turbines, resulting in higher operating pitch angles hence reduced normal force components, while the aligned turbines were operating close to rated speed where the thrust force is maximum. Overall the staggered layout seemed to prevail in terms of wind potential and fatigue loading, yet more parameters have to be checked such as

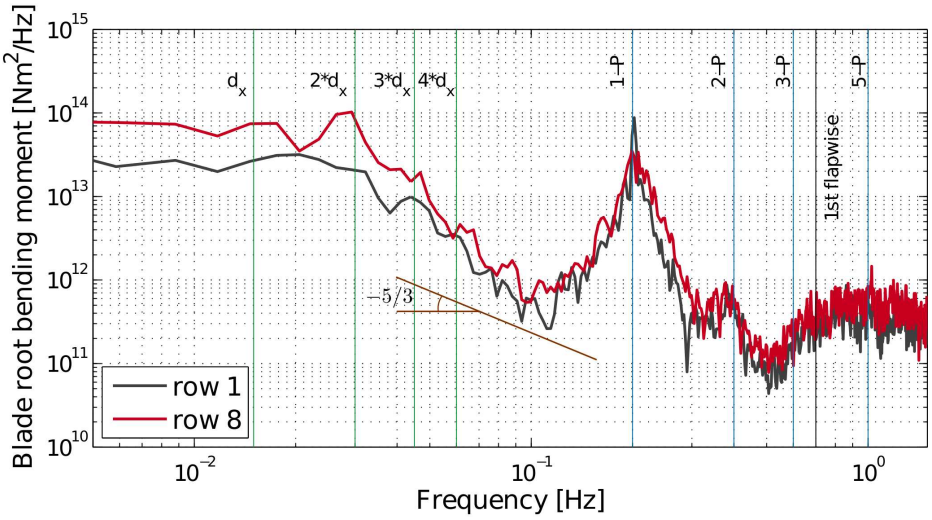

Figure 7. Power spectral density of the out-of-plane blade root bending moment of a turbine located in first and eighth row. The vertical green lines represent the transit time for the flow to reach a downstream row, where d_x is the streamwise spacing between two rows. The vertical blue lines represent the once-per-revolution (1-P) frequency and its harmonics, while the vertical black line shows the frequency of the first flapwise bending mode.

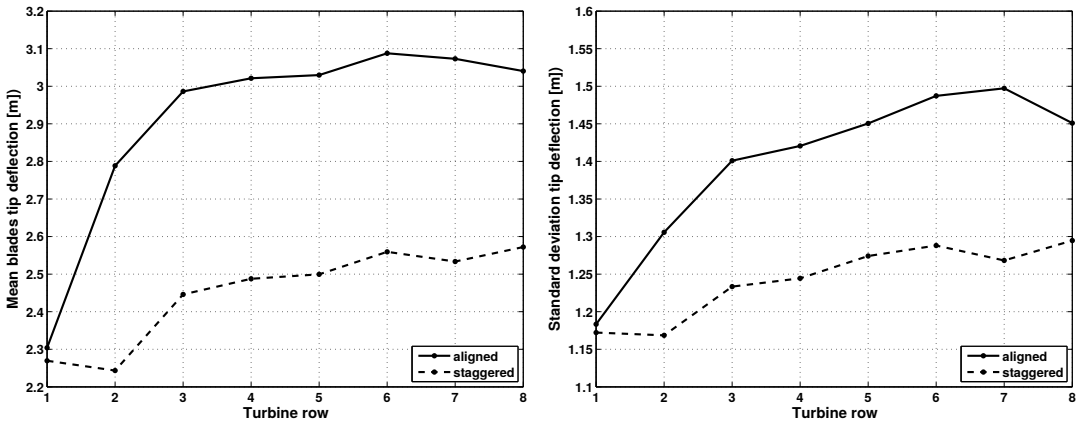

Figure 8. Mean (left) and standard deviation (right) of the time and row-averaged out-of-plane blades tip deflection for the two wind farm layouts.

wind direction, flow regime, turbine spacing, and may comprise the subject of a future study.

Acknowledgments

The authors acknowledge support from the European Research Council (FP7–Ideas, grant no. 306471). Simulations were performed on the computing infrastructure of the VSC Flemish Supercomputer Center, funded by the Hercules Foundation and the Flemish Government.

References

[1] V.S. Bokharaie, P. Bauweraerts, and J. Meyers. Wind-farm layout optimisation using a hybrid Jensen-LES approach. *Wind Energy Science Discussions*, 2016:1–23, 2016.

[2] J.P. Goit and J. Meyers. Optimal control of energy extraction in wind-farm boundary layers. *Journal of Fluid Mechanics*, 768:5–50, 2015.

[3] P.A. Fleming, P.M.O. Gebraad, S. Lee, J.W. van Wingerden, K. Johnson, M. Churchfield, J. Michalakes, P. Spalart, and P. Moriarty. Evaluating techniques for redirecting turbine wakes using SOWFA. *Renewable Energy*, 70:211 – 218, 2014.

[4] M. Soleimanzadeh, R. Wisniewski, and S. Kanev. An optimization framework for load and power distribution in wind farms. *Journal of Wind Engineering and Industrial Aerodynamics*, 107108:256 – 262, 2012.

[5] Robert Mikkelsen. *Actuator disk methods applied to wind turbines*. PhD thesis, Technical University of Denmark, Lyngby, Denmark, 2003.

[6] Stefan S.A. Ivanell. *Numerical computations of wind turbine wakes*. PhD thesis, KTH Royal Institute of Technology, Stockholm, Sweden, 2009.

[7] M. Calaf, C. Meneveau, and J. Meyers. Large eddy simulation study of fully developed wind-turbine array boundary layers. *Physics of Fluids*, 22(1), 2010.

[8] M. Calaf, M.B. Parlange, and C. Meneveau. Large eddy simulation study of scalar transport in fully developed wind-turbine array boundary layers. *Physics of Fluids*, 23(12), 2011.

[9] J. Meyers and C. Meneveau. Optimal turbine spacing in fully developed wind farm boundary layers. *Wind Energy*, 15(2):305–317, 2012.

[10] J.N. Sørensen and W.Z. Shen. Numerical modeling of wind turbine wakes. *Journal of Fluids Engineering*, 124(2):393–399, 2002.

[11] Niels Troldborg. *Actuator Line Modeling of Wind Turbine Wakes*. PhD thesis, Technical University of Denmark, Lyngby, Denmark, 2009.

[12] F. Porté-Agel, Y.T. Wu, H. Lu, and R.J. Conzemius. Large-eddy simulation of atmospheric boundary layer flow through wind turbines and wind farms. *Journal of Wind Engineering and Industrial Aerodynamics*, 99(4):154 – 168, 2011. The Fifth International Symposium on Computational Wind Engineering.

[13] H. Lu and F. Porté-Agel. Large-eddy simulation of a very large wind farm in a stable atmospheric boundary layer. *Physics of Fluids*, 23(6), 2011.

[14] M. Churchfield, S. Lee, P. Moriarty, L. Martinez, S. Leonardi, G. Vijayakumar, and J. Brasseur. A large-eddy simulations of wind-plant aerodynamics. Proceedings of the AIAA Aerospace Sciences Meeting, Nashville, Tennessee, USA, 2012.

[15] I. Dobrev, F. Massouh, and M. Rapin. Actuator surface hybrid model. *Journal of Physics: Conference Series*, 75(1):012019, 2007.

[16] R.C. Storey, S.E. Norris, and J.E. Cater. An actuator sector method for efficient transient wind turbine simulation. *Wind Energy*, 18(4):699–711, 2015.

[17] A. Ahlström. Influence of wind turbine flexibility on loads and power production. *Wind Energy*, 9(3):237–249, 2006.

[18] S.J. Andersen, B. Witha, S.P. Breton, J.N. Sørensen, R.F. Mikkelsen, and S. Ivanell. Quantifying variability of large eddy simulations of very large wind farms. *Journal of Physics: Conference Series*, 625(1):012027, 2015.

[19] J.N. Sørensen, R.F. Mikkelsen, D.S. Henningson, S. Ivanell, S. Sarmast, and S.J. Andersen. Simulation of wind turbine wakes using the actuator line technique. *Philosophical Transactions of the Royal Society of London A: Mathematical, Physical and Engineering Sciences*, 373(2035), 2015.

[20] R.C. Storey, S.E. Norris, K.A. Stol, and J.E. Cater. Large eddy simulation of dynamically controlled wind turbines in an offshore environment. *Wind Energy*, 16(6):845–864, 2013.

[21] J.M. Jason and M.L. Buhl Jr. Fast users guide. Technical Report NREL/EL-500-38230, August 2005.

[22] R.C. Storey, J.E. Cater, and S.E. Norris. Large eddy simulation of turbine loading and performance in a wind farm. *Renewable Energy*, 95:31 – 42, 2016.

[23] H.G. Weller, G. Tabor, H. Jasak, and C. Fureby. A tensorial approach to computational continuum mechanics using object-oriented techniques. *Comput. Phys.*, 12(6):620–631, November 1998.

[24] M.J. Churchfield, S. Lee, J. Michalakes, and P.J. Moriarty. A numerical study of the effects of atmospheric and wake turbulence on wind turbine dynamics. *Journal of Turbulence*, 13:N14, 2012.

[25] J. Nathan, C. Masson, L. Dufresne, and M. Churchfield. Analysis of the sweeped actuator line method. *E3S Web of Conferences, 2nd Symposium on OpenFOAM in Wind Energy*, 5:01001, 2015.

[26] W. Munters, C. Meneveau, and J. Meyers. Shifted periodic boundary conditions for simulations of wall-bounded turbulent flows. *Physics of Fluids*, 28(2), 2016.

[27] P.J. Mason and D.J. Thomson. Stochastic backscatter in large-eddy simulations of boundary layers. *Journal of Fluid Mechanics*, 242:51–78, 9 1992.

[28] A.A. Shabana. *Dynamics of Multibody Systems*. Cambridge University Press, 2013.

[29] A.A. Shabana and R. Schwertassek. Equivalence of the floating frame of reference approach and finite element formulations. *International Journal of Non-Linear Mechanics*, 33(3):417 – 432, 1998.

[30] J. Jonkman, S. Butterfield, W. Musial, and G. Scott. Definition of a 5-MW reference wind turbine for offshore system development. Technical report, National Renewable Energy Laboratory, 2009.
[31] J.S. Przemieniecki. *Theory of Matrix Structural Analysis*. McGraw-Hill, New York, 1968.
[32] A.A. Nada, B.A. Hussein, S.M. Megahed, and A.A. Shabana. Use of the floating frame of reference formulation in the large deformation analysis: Experimental and numerical validation. *Pro. IMechE, Part K: Journal of Multi-body Dynamics*, 224:45–58, 2009.
[33] E.A. Bossanyi. Wind turbine control for load reduction. *Wind Energy*, 6(3):229–244, 2003.
[34] M. Arnold and O. Brüls. Convergence of the generalized-α scheme for constrained mechanical systems. *Multibody System Dynamics*, 18(2):185–202, 2007.
[35] C.A. Felippa, K.C. Park, and C. Farhat. Partitioned analysis of coupled mechanical systems. *Computer Methods in Applied Mechanics and Engineering*, 190(2425):3247 – 3270, 2001.
[36] H.J. Sutherland. Fatigue analysis of wind turbines. Technical report, Sandia National Laboratories, 1999.
[37] S.D. Downing and D.F. Socie. Simple rainflow counting algorithms. *International Journal of Fatigue*, 4(1):31 – 40, 1982.
[38] G. Freebury and W. Musial. Determining equivalent damage loading for full-scale wind turbine blade fatigue tests. Proceedings of the AIAA Aerospace Sciences Meetings, Reno, NV, USA, 2000.
[39] J. Bossuyt, M. Howland, C. Meneveau, and J. Meyers. Measuring power output intermittency and unsteady loading in a micro wind farm model. 34th Wind Energy Symposium, AIAA SciTech, 2016.